Metabolism modulates global synchrony in the aging brain

Corey Weistuch[a,b], Lilianne R Mujica-Parodi[a,c,d,e,f], Anar Amgalan[a,c,e], Ken A Dill[a,e,g,*]

[a] *Laufer Center for Physical and Quantitative Biology, Stony Brook University, Stony Brook, USA*
[b] *Department of Applied Mathematics and Statistics, Stony Brook University, Stony Brook, USA*
[c] *Department of Biomedical Engineering, Stony Brook University, Stony Brook, USA*
[d] *Program in Neuroscience, Stony Brook University, Stony Brook, USA*
[e] *Department of Physics and Astronomy, Stony Brook University, Stony Brook, USA*
[f] *Athinoula A. Martinos Center for Biomedical Imaging, Massachusetts General Hospital and Harvard Medical School, Boston, USA*
[g] *Department of Chemistry, Stony Brook University, Stony Brook, USA*

Abstract

Brain aging is associated with hypometabolism and associated global changes in functional connectivity. Using fMRI, we show that brains become globally desynchronized with age. Applying quantitative methods from statistical physics, our data identify synchrony patterns in the healthy brain to be poised at a critical point between segregating and integrating functions. We further show that aging shifts the brain away from this critical point, making it possible for marked threshold changes at the whole brain scale to arise as emergent properties of minute continuous changes in metabolism at the neuronal scale. Finally, by experimentally modulating metabolism at the neuronal scale in younger adults, we establish that this variable alone–independent of age–can provide a mechanism for global changes in synchrony.

Keywords:

fMRI, Aging, Neurometabolism, Synchrony, Ising Model, Criticality

*Corresponding Author: Ken A Dill, Laufer Center for Physical and Quantitative Biology, Stony Brook University, 100 Nicolls Rd, Stony Brook, USA, 11794; Email, dill@laufercenter.org

1. Introduction

An important question is how the familiar patterns of *macroscale*, brain-wide activity arise from the *microscale* properties of the constituent neurons and their networks. Here, our interest is in aging brains. We study how the brain's global activity patterns change with age, and how those changes can arise from the reduced metabolic activity of the constituent microscopic regions.

We draw on two types of experimental evidence. First, aging is associated with weakened *functional connectivity* (FC), *i.e.* reduced communication between brain regions [1, 2, 3], as shown by functional magnetic resonance imaging (fMRI). Second, older brains show reduced glucose metabolism in positron emission tomography (PET) experiments [4, 5, 6]. Combining these observations has led to the hypothesis that reduced metabolism underlies the observed changes in FC [4, 7]. Indeed, similar disruptions have been observed in Type 2 diabetic subjects [8, 9].

At rest (i.e., when no explicit task is being done), brain activity alternates between *segregating* computations to localized functional domains and *integrating* this information across these domains [7, 10, 11, 12]. Metabolic demand increases in proportion to the number and length of functional connections [13], making highly-connected functional networks more energetically costly [10]. Such connections are the first to weaken with age [3, 7, 14]. Thus, declining glucose metabolism in older brains would seem to bias brain activity to selectively utilize lower-cost, segregated networks.

Here, we develop a model to explore this hypothesis quantitatively. In particular, there is a question of amplification. Changes in metabolism are minute and incremental with age, while changes in functional connectivity – from more integrated in the young to more segregated in the old – are relatively marked and abrupt. The approach of choice to understand how these sharp changes arise is statistical mechanics, which interprets the properties of complex systems in terms of collective interactions between the underlying parts [15]. Indeed, am-

plification from the micro to macro scale is commonly seen in phase transitions and critical phenomena. Here the macroscopic property of interest is the network *synchrony*, a time-dependent average of the activity over the entire brain [16, 17, 18]. Thus, we employ here an *Ising model* [18, 19, 20] of networks to explore how small changes in neuronal metabolism with age could lead to large, global changes in brain synchrony.

We analyzed two fMRI datasets that vary metabolism at the between-subject and within-subject levels, respectively. The first is the *lifespan* Cam-CAN 3T fMRI resting-state dataset of 636 individuals, ranging over ages 18-88 [21]. The second, in which we hold age constant in order to isolate the effects of energy alone, is the *metabolic* PAgB 7T fMRI within-subject experiment of 12 healthy young adults scanned while on glycolytic and ketogenic diets [22]. Ketone bodies increase the Gibbs free energy change rate of ATP production by 27% as compared to glucose [23], with associated increases in cardiac efficiency [23] and brain activity [22]. Thus, if features of functional connectivity seen in older brains result from reduced metabolism, then switching the brain's metabolism from a state of lower Gibbs free energy (glucose) to higher Gibbs free energy (ketones) should shift those features in the opposite direction.

2. Methods

2.1. Lifespan and metabolic neuroimaging datasets

To identify fMRI synchrony across the lifespan, we analyzed a large-scale 3T fMRI resting-state dataset: the Cambridge Centre for Ageing and Neuroscience stage II (Cam-CAN: ages 18-88, $N = 636$) [21]. The Cam-CAN study was designed to identify neural correlates of normal aging and provided a roughly uniform coverage of age groups, allowing comparison between groups as well as a wide array of behavioral measures. While the functional MRI imaging of Cam-CAN stage II included both task and resting-state data, for our analyses we used only the resting-state data. To determine how energy availability (metabolism)

affects fMRI synchrony, we additionally analyzed data from a within-subject experiment from the Protecting the Aging Brain (PAgB) database [22] in which young healthy adults ($N = 12$, $\mu_{age} = 28\pm$ 6.73 years; 4 female) were scanned at resting-state under two conditions: (1) *glycolytic*, following their standard diet, without fasting; and (2) *ketogenic*, following a high-fat, moderate-protein, low-carbohydrate ($<$ 50 g/day) diet for one week, by which point all participants were in ketosis ($>$ 0.6 mmol/L ketone blood concentration). For details on the glycolytic and ketogenic dietary regimes, as well as validation of their blood values and neurobiological effects as comparable to calorie-matched administration of glucose and D-β-hydroxybuterate ketone bodies, see previous work [22]. *Studies were approved by the Institutional Review Boards of Cambridge University and Massachusetts General Hospital/Partners Healthcare, respectively; all participants provided informed consent.*

2.2. MRI acquisition

The Cam-CAN lifespan dataset includes multiple imaging modalities (T1 and T2-weighted images, diffusion-weighted images, BOLD EPI images during tasks of 3 varying levels of cognitive demand, MEG images during 2 separate cognitive loads and magnetisation-transfer images). Of these, the resting-state BOLD EPI fMRI was the focus of our analysis (full dataset documentation at [21]). The Cam-CAN functional imaging was done at 3T field strength, with TR=1970 ms over 8 min 40 s. The neuroimaging experiments of Cam-CAN study were conducted in Cambridge, UK at the Medical Research Council Cognition and Brain Sciences Unit (MRC-CBSU). Specifics of the BOLD EPI imaging protocol included: TR = 1970 ms, TE = 30 ms, flip angle = 78°, voxel size = $3 \times 3 \times 4.44$ mm, slices = 32, number of measurements = 261. The PAgB metabolic dataset was acquired at ultra-high-field (7T) field strength at the Athinoula A. Martinos Center for Biomedical Imaging. Imaging included whole brain BOLD, field map, and T1-weighted structural (MEMPRAGE) images. BOLD images were acquired using a protocol quantitatively optimized, using a dynamic phantom, for detection-sensitivity to resting-state networks [24]: SMS

slice acceleration factor = 5, R = 2 acceleration in the primary phase encoding direction (48 reference lines) and online GRAPPA image reconstruction, TR = 802 ms, TE = 20 ms, flip angle = 33°, voxel size = $2 \times 2 \times 1.5$ mm, slices = 85, number of measurements = 740 in each resting-state session, for a total acquisition time of 10 minutes. Field map images were acquired using the following parameters: TR = 723 ms, TE 1 = 4.60 ms, TE 2 = 5.62 ms, flip angle = 36°, voxel size = $1.7 \times 1.7 \times 1.5$ mm, slices = 89, for a total acquisition time of 3 min 14 s. The whole-brain T1-weighted structural volumes were acquired using a conventional multi-echo MPRAGE (MEMPRAGE) sequence with 1 mm isotropic voxel size and four echoes with the following protocol parameters: TE1 = 1.61 ms, TE2 = 3.47 ms, TE3 = 5.33 ms, TE4 = 7.19 ms, TR = 2530 ms, flip angle = 7°, with R = 2 acceleration in the primary phase encoding direction (32 reference lines) and online GRAPPA image reconstruction, for a total volume acquisition time of 6 min 3 s.

2.3. MRI pre-processing

Lifespan dataset pre-processing was conducted in FMRIB Software Library (FSL; https://fsl.fmrib.ox.ac.uk/fsl/fslwiki/) and FreeSurfer (https://surfer.nmr.mgh.harvard.edu/): anatomical images were skull-stripped using FreeSurfer and co-registered to Montreal Neurological Institute (MNI) templates and mean functional images using FLIRT (part of FSL). Functional images were motion and fieldmap-corrected (using MCFLIRT and epidewarp), brain-extracted (using BET), and co-registered to MNI templates using transformations learned through the anatomical image. Motion parameter as well as tissue segmentation-extracted white-matter and CSF confounds (using FAST) were regressed out at ROI-level time-series extraction stage using nilearn package (https://nilearn.github.io) [25]. Metabolic dataset pre-processing used Statistical Parametric Mapping 12 (SPM12; https://www.fil.ion.ucl.ac.uk/spm/software/spm12/) was used as in our previous studies conducted at the same acquisition parameters [26], [22]. Anatomical images (MEMPRAGE) were normalized to MNI templates using unified segmentation and registration. Images of each individual participant

were realigned to account for head movements, and fieldmap-corrected (using epidewarp.fsl) for geometric distortions caused by the magnetic field inhomogeneity. Following normalization, structural images were probabilistically segmented into 3 tissues: grey and white matters and CSF. We did not apply spatial smoothing or global signal regression to pre-processing of either dataset. For all datasets, voxelwise data were parceled into the Willard 499 functional regions of interest (ROI) [27]. Of these, we used the 498 regions corresponding to entirely grey matter voxels.

2.4. Ising model

Here we use the principle of maximum entropy [18, 20, 28] to build the minimally biased probability distribution of N binary ($+1$ or -1) node weights, $\{\hat{v}_i\}$ satisfying fixed constraints on the mean (0) and variance, $Var(s)$ of the global property, $s(\{\hat{v}_i\}) = N^{-1}\sum_{i=1}^{N}\hat{v}_i$ (synchrony). This is given by [28]:

$$P(\{\hat{v}_i\}) = Z^{-1}e^{N^2\lambda s(\{\hat{v}_i\})^2} \tag{1}$$

where Z is the partition function and normalizes the distribution. Here λ represents the average node-to-node interaction strength and is the basic mechanistic quantity of our model (**Fig. 1a, left**). Small values of λ describe networks in which interactions between nodes are weak and in which the node weights are independent of each other. In contrast, large values of λ describe networks in which interactions between nodes are strong and node activities are highly correlated (**Fig. 1a, right**). A given value of synchronization s may be obtained in many different ways; *ie,* it is *degenerate* (**Fig. 1b**). In other words, since there are $\binom{N}{N(1+s)/2}$ different ways to have $s = N^{-1}\sum_i \hat{v}_i$, we find that the total probability of each synchrony $P(s)$ is:

$$P(\{\hat{v}_i\}) = Z^{-1}\binom{N}{N(1+s)/2}e^{N^2\lambda s(\{\hat{v}_i\})^2} \tag{2}$$

Therefore, when λ is small, $P(s)$ is determined by the degeneracy and low synchrony is most probable. Conversely, when λ is large, $P(s)$ is determined by the interactions between nodes and high synchrony is most probable. In particular,

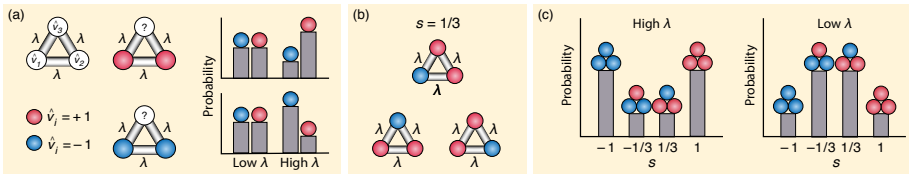

Figure 1 The Ising model predicts network probabilities from interactions between its nodes. (**a**) The Ising model maps binary variables onto a fully-connected network (**left**). Each variable ($i = 1,2,\ldots$ N) is a node with binary weight $\hat{v}_i$ (represented by the colors red and blue), and each pair of nodes is connected by an edge with weight λ. Here we show the example of $N = 3$. The value of λ (> 0) describes the average interaction strength between nodes; the larger λ is, the more likely the unknown value of $\hat{v}_3$ is to be similar to its neighbors (**right**). (**b,c**) The probability of each network is determined by its synchrony (s). (**b**) Multiple graphs give the same value of synchrony. Since there are 3 ways to have 1 blue node and 2 red nodes, there are 3 different graphs that give $s = 1/3$ (red minus blue divided by $N = 3$). This *degeneracy* effectively triples the probability of $s = 1/3$. (**c**) The probability distribution of s given by the Ising model is a function of λ and degeneracy. When λ (interaction) is high, the probability that $|s| = 1$ is large (**left**). But, when λ is low, degeneracy wins out and the probability that $|s| = 1/3$ is large (**right**).

as the λ is varied, the relative importance of each of these terms changes. As can be seen in **Fig. 1c**, this causes $P(s)$ to change from a bimodal (left) to a unimodal (right) distribution as depending on λ. The critical point, λ_c, is the value of λ where this shift happens (i.e. when these two contributions are balanced). Using the standard approximation of the binomial coefficients, $P(s)$ becomes:

$$P(s) \approx Z^{-1}\binom{N}{N/2}e^{[\lambda-\frac{1}{2N}]s^2} \tag{3}$$

Conceptually, when $\lambda < \lambda_c$, P(s) opens downwards like a Gaussian; $s = 0$ is most probable. However, when $\lambda > \lambda_c$, $P(s)$ opens upwards and large values of s (both positive and negative) are most probable. When $N = 498$ (the number of regions), we find that this critical point is $\lambda_c = \frac{1}{2N} = 1.004 \times 10^{-3}$, coinciding with the observed transition between unimodal and bimodal synchrony (**Fig. 1c**). To simplify our analysis, now refer to the rescaled coupling Λ: $\Lambda = (\lambda - \lambda_c)/\lambda_c$.

2.5. fMRI binarization

Here we access the time-dependent network properties of our data by binarizing fMRI time series. This method simplifies time series while preserving their correlation patterns. In particular, the Pearson correlation (or functional connectivity), $\rho(X, Y)$ is widely used to estimate the strength of the interaction between arbitrary pairs of variables (X,Y):

$$\rho(X, Y) = \frac{Cov(X, Y)}{\sqrt{Var(X)Var(Y)}}. \tag{4}$$

Here variables (X and Y for example) are the nodes of a graph and ρ is the weight of the edge between them. However, these interactions often change over time [29]. Thus, we calculate ρ over each pair of successive time points, reducing Eq. 4 to:

$$\begin{aligned} \rho^*(X, Y, t) =& \frac{\Delta X(t)\Delta Y(t)}{\sqrt{(\Delta X(t))^2(\Delta Y(t))^2}} = \hat{X}(t)\hat{Y}(t) \\ BDM(X, t) =& \hat{X}(t) \end{aligned} \tag{5}$$

where $\hat{X}$ and $\hat{Y}$ are the signs of the time derivatives of X and Y respectively and the time-dependent correlation, ρ^*, is their product. This procedure takes our original time series $X(t)$ and produces a simplified, binarized time series $\hat{X}(t)$ (*Binarized Derivative Method*, BDM). As validation of this method, we find that this simplified representation preserves fMRI correlation patterns across time (*Supplementary Fig. 1a*) and for different subjects (*Supplementary Fig. 1b*). This approach has two key advantages over previous methods [29, 30]. First, it simplifies complex, many-variable interactions in terms of dynamical patterns of binary ($+1$ and -1) variables. Second, it is naturally compatible with Ising-like models, which have been shown to be powerful tools in isolating latent relationships within networks of neurons [20, 28].

2.6. Model fitting

Here we describe how we fit the Ising model to our data (**Fig. 2**). First, we took the fMRI signal $v_i(t)$ for each region i and time t and binarized it using

BDM. The model assumes that all nodes have, on average, similar correlation patterns. We tested this assumption by computing the total (over all pairs) functional connectivity for each region. Here, we used the subject-averaged (over all diets and ages) functional connectivity matrix as our reference (*Supplementary Fig. 2*). From these signals, we found that most nodes are primarily positively correlated, while a few nodes were primarily negatively correlated with other nodes. For the latter, we flipped ($\hat{v}_i \to -\hat{v}_i$) for these regions only in order to satisfy the assumptions of our Ising model (*Supplementary Fig. 2*). For each subject, we then computed the time-dependent *synchrony* $s(t)$ (each TR is a time point) using the binarized fMRI signals from all (498) regions of the brain. We then took the histogram of $s(t)$ for each subject to get a distribution $P(s)$, giving the variation in synchrony per individual. This was then used to obtain Λ by fitting $P(s)$ to the Ising model Eq. 2. This fit is expressed by the Bayesian posterior distribution $P(\Lambda|\text{Data})$, which captures the relative quality of of our model. Here we use a uniform (unbiased) prior distribution of Λ; thus the posterior is computed directly from the likelihood function $\mathcal{L}(\Lambda|\text{Data})$ of our Ising model **Eq. 2.** In practice, we will summarize this posterior by its peak (the maximum likelihood estimate) and its width (0.01 likelihood ratio error bars).

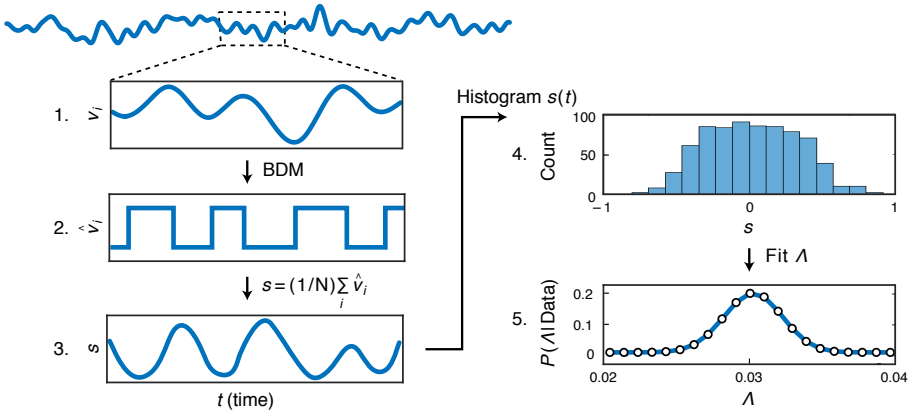

Figure 2 How we obtain the Ising model parameter Λ from fMRI data. [1] shows the fMRI signal $v_i(t)$ from the ith brain region (out of 498), as a function of time t. [2] We binarize it, to give $\hat{v}_i(t)$. [3] The binarized signals are then averaged over all brain regions, giving that individual's time-dependent *synchrony* $s(t)$. [4] We then histogram into $P(s)$ the different s values over time [4], to express the variations in an individual's synchrony levels. [5] We then find the value of Λ that best fits $P(s)$ for each individual. Here $P(\Lambda|\text{Data})$ expresses the Bayesian posterior probability (with a uniform prior distribution over Λ) that our data $P(s)$ was generated from an Ising model (**Eq. 2**) with relative interaction strength Λ.

3. Results

To interpret our fMRI data, we developed a generative biophysical approach based on a network *Ising model* [19, 20]. Widely used in physics, the Ising model is the simplest model describing how pairwise interactions (or couplings) among microscopic, binary (± 1) elements give rise to macroscopic behaviors, including correlations ([19], **Fig. 1**). Here our microscopic elements are the 498 Willard Atlas brain regions measured in fMRI experiments, each of which is initially assumed to be connected to every other with the same coupling strength (*Supplementary Fig. 2*). The "macroscopic" behavior of interest is the observed network *synchrony*, s, or the average activity across all regions [27, 28]. To explore this model, we find the value of the relative coupling, Λ, that best fits the experimentally observed synchrony values for each subject (**Fig. 2**). Here, each value of s corresponds to the degree of order of a particular network produced by the best-fitting Ising model [28]. As further validation for our model, we find that the Ising model, regardless of age and metabolic condition,

correctly captures the kurtosis of $P(s)$. a higher-order feature that cannot be predicted from correlations alone (*Supplementary Fig. 3*). Thus, we use Λ to learn how synchrony depends on both age and available energy.

Ising models are useful in understanding how small changes in microscopic properties (such as a coupling) can give rise to abrupt and qualitatively distinct macroscopic changes (i.e., emergent effects). The node-node couplings (assumed positive) control the occupation probabilities of different networks. When couplings (Λ) are large, ordered networks ($s = \pm 1$) are most likely (**Fig. 3**, orange), and when they are small, random disordered networks ($s = 0$) are most likely (**Fig. 3**, blue). Much like water at its boiling point, which discontinuously changes from liquid to vapor, the transition between these cases is sharp and occurs at a coupling of intermediate strength, called the *critical point*. Here we use Λ to denote the deviation from the critical point. While both ordered and disordered networks are equally likely at the critical point (**Fig. 3**, red, $\Lambda = 0$), small changes in the couplings lead to large changes in the occupation probabilities.

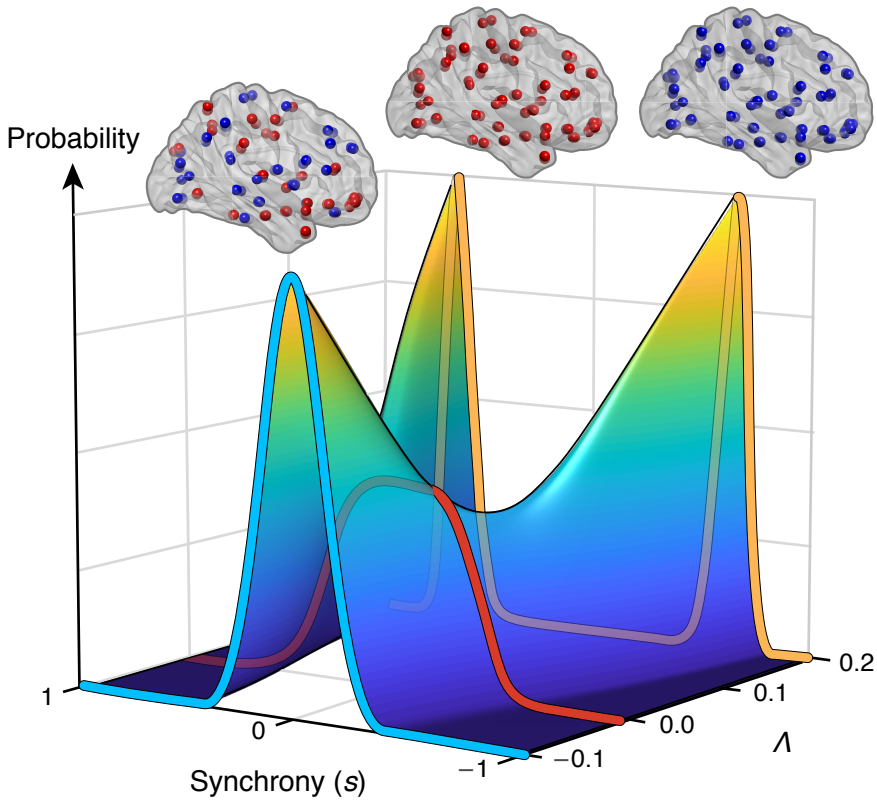

Figure 3 The Ising model applied to brain synchrony. Shown is the probability distribution of different values of synchrony (s) for different values of the dimensionless quantity Λ, reflecting the distance of the actual coupling, λ from the critical point λ_c: $\Lambda = (\lambda - \lambda_c)/\lambda_c$. For $\Lambda < 0$ (weak coupling), there is a single unimodal population having a peak at $s = 0$ (blue line). For $\Lambda > 0$ (strong coupling), the population is bimodal, with a peaks at $s \gg 0$ and $s \ll 0$ (orange line). Above each peak is a typical network; nodes are brain regions and colors are states (red $+1$, blue -1). $\Lambda = 0$ defines the critical point, where $s = 0$ changes from a minimum to a maximum and P(s) rapidly changes (red line). At the critical point, low and high synchrony networks are equally probable.

To establish the relationship between synchrony and the occupation probabilities of different functional networks, we separately computed the inter-subject average functional connectivity matrices during periods of low and high synchrony. During periods of low synchrony, functional connections are found to be sparse and segregated (**Fig. 4a**, Seg), while during high synchrony, they are dense and integrated (**Fig. 4b**, Int) [10]. Thus, our model explains the changes in observed FC patterns in terms of relative amounts of underlying segregated versus integrated activity. Consequently, just as with synchrony (**Fig. 3**), different values of Λ change the relative time spent in segregated (P_{Seg}) and integrated (P_{Int}) networks (**Fig. 4c**, $R^2 > 0.9$, sigmoidal fit not shown, each colored marker is a subject), independent of age or available energy. Here, the time spent in each pattern was computed as the similarity of each subject's FC to the extracted patterns, Int and Seg. When $\Lambda < 0$, low synchronies and segregated networks occur more frequently, while the opposite holds when $\Lambda > 0$. In both cases, this balance rapidly shifts at the critical point, $\Lambda = 0$.

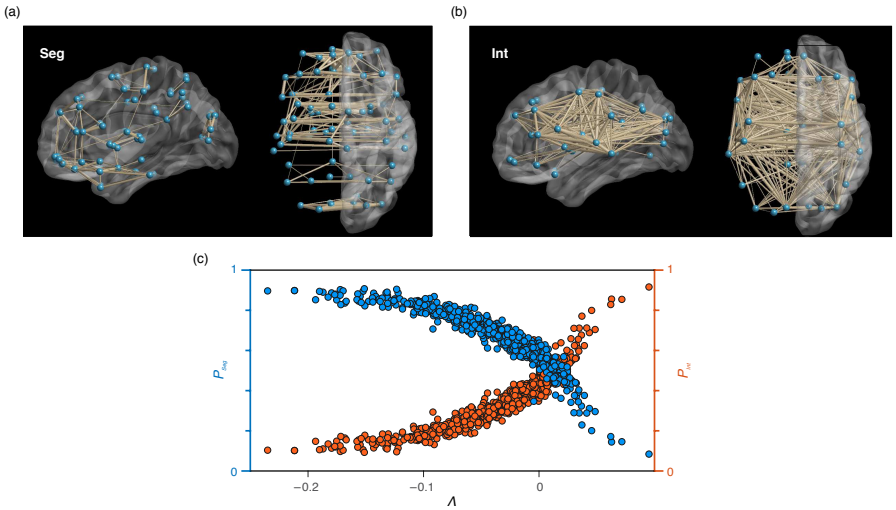

Figure 4 Λ controls the balance between segregated (low s) and integrated (high s) networks. (**a,b**) Inter-subject average functional connectivity (Pearson Correlation) during low (**a**) and high (**b**) synchrony, here visualized using the BrainNet Viewer showing the top 10 % of connections [31]. (**a**) Low synchrony ($s = 0$) reflects segregation (Seg). (**b**) High synchrony ($|s| > 1/2$) reflects integration (Int). (**c**) The fraction of time each subject (each data point and their specific value of Λ) spends in integrated (P_{Int}, orange) and segregated (P_{Seg}, blue) networks. Time spent was calculated from a bivariate regression of the functional connectivity (here over all s, from each subject) with the patterns, Seg and Int. $\Lambda < 0$ corresponds to large P_{Seg} and small P_{Int} while $\Lambda > 0$ corresponds to the opposite. The cross-over in (**c**) occurs at the critical point, $\Lambda = 0$.

Changes in FC with both age and available energy can be described by changes in the region-region coupling Λ. In particular, we find that Λ significantly decreases with age ($p = 1.7 \times 10^{-38}$, $N = 636$, **Fig. 5a**), suggesting that aging is associated with a marked shift from integrated towards more segregated network activities. But, upon switching from a lower-energy glucose to a higher-energy ketone metabolism, Λ increases ($p = 1,2 \times 10^{-3}$, $N = 12$, **Fig. 5b**) by about 25% to 50% of the decrease seen over the entire lifespan. Thus, by toggling the relative frequencies of segregated and integrated networks, Λ reflects an average cost of functional activity and, as suggested by our metabolic experiment, the amount of energy available to the brain. Thus one way the brain may conserve energy when this amount of energy available is decreased, such as through aging, is by decreasing Λ.

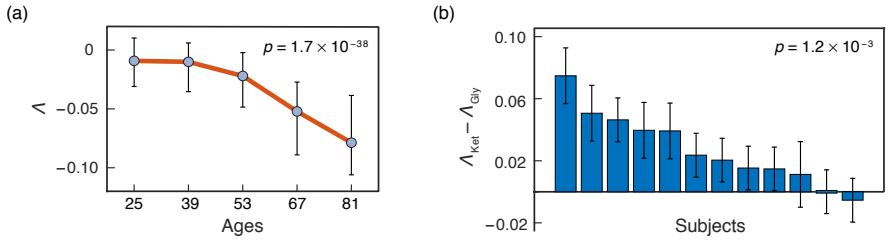

Figure 5 Λ significantly decreases with age (**a**, $p = 1.7 \times 10^{-38}$) and increases with available energy (**b**, $p = 1.2 \times 10^{-3}$). (**a**) Here each point (as well as the orange curve connecting them) reflect the median best-fit Λ values for each (of 5) equal width (14 years) age groups. Error bars represent the upper and lower quartiles. We used a Spearman-rank Permutation test ($N = 636$, $\rho(634) = -0.48$) to test significance of the nonlinear relationship between Λ and age. (**b**) Change in Λ for each subject ($N = 12$, $W = 3$) when switching from a lower-energy glucose (glycolytic, Gly) to higher energy ketone (Ket) metabolism. Error bars reflect a 0.01 likelihood ratio confidence interval. A Wilcoxon 1-sided signed rank test ($N = 12$) was used to test if ketones significantly increased Λ.

But why does a small change in energy availability lead to the dramatic changes in FC seen in older age? A third principal finding here is that young healthy brains are poised at a *critical point*, whereby very small changes in the coupling strength between regions leads to a sharp transition between integrated and segregated networks [19, 20]. **Figure 6** expresses this in terms of the probability distribution of s, now viewed from the top-down. Here younger brains (green, age 25 ± 7) are near the critical point (black), allowing them to access both high and low synchrony networks. But as energy availability decreases, such as in older brains (yellow, age 81 ± 7), the resulting decrease in Λ causes the probabilities of higher synchrony networks to quickly fall to 0.

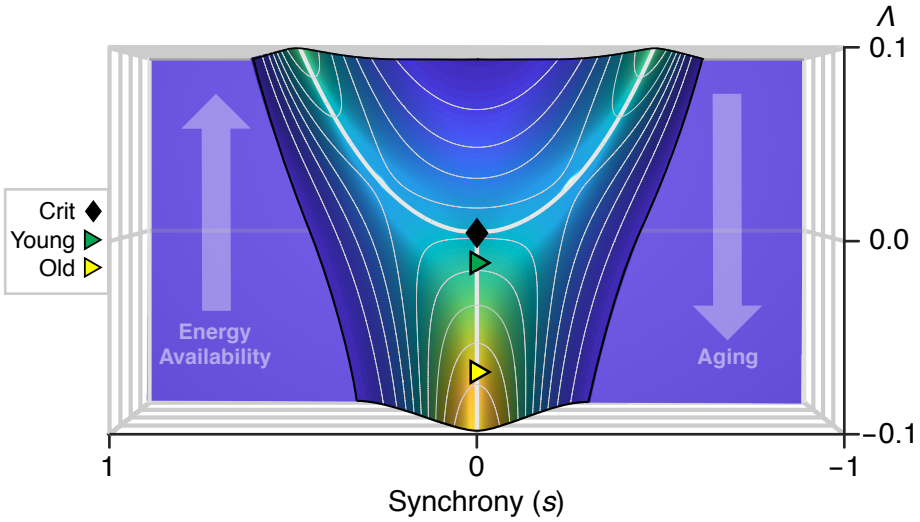

Figure 6 Younger brains are poised at a critical point; this is disrupted by decreasing energy availability. Shown is the probability distribution of synchrony (s) vs Λ, viewed from the top-down. At the critical point ($\Lambda = 0$, black), peak synchrony (indicated by a white line) changes from low ($s = 0$) towards high ($s < 0$ and $s > 0$) values. Near this transition, such as seen in younger brains (Age 25 ± 7, $N = 85$, green), both low and high synchrony networks can be accessed. Reducing metabolic activity causes Λ to decrease. Older brains (Age 81 ± 7, $N = 121$, yellow) have smaller Λ and only access low synchrony networks. The plotted triangles correspond to the Λ values centered at ages 25 (Young) and 81 (Old) (**Fig. 5**).

4. Discussion

Our results show that metabolic disruptions in the aging brain lead to a dramatic decrease in whole-brain synchrony. Thus, our results suggest that metabolism may modulate the strength of synaptic connections in ways that affect BOLD connectivity, an important direction for future experiments that is additionally supported by two mechanistic results. First, BOLD connectivity has been shown to result from the strength of neuronal synaptic connections[16]. Second, because of its especially large metabolic cost, synaptic connectivity is severely disrupted by decreased energy supply [32, 33, 34, 35]. Thus, extension of our current paradigm to older populations may provide crucial data to establish the direction of causality between two neurological hallmarks of brain aging: the progressive weakening of synaptic connectivity[36, 37] and the gradual loss of ability to metabolize glucose. Specifically, if glucose hypometabolism underlies loss of synaptic connectivity, which in turn drives loss of BOLD connectivity, then administration of exogenous ketones should improve fMRI synchrony in older adults. In contrast, if loss of synaptic connectivity underlies glucose hypometabolism, which in turn drives loss of BOLD connectivity, then administration of exogenous ketones should not improve fMRI synchrony in older adults.

That brains at their presumed peak of functionality should be poised so close to a critical point of synchrony may reflect a cost-benefit trade-off. If interactions were too weak (negative Λ, unimodal distributions around $s = 0$, no integration), the brain would have low functionality since a typical region could not access much of the rest of the brain. In contrast, if interactions were too strong (positive Λ, bimodal distributions, large positive and negative s values, no segregation), it would be metabolically expensive to run and non-specialized. By being poised at the critical point, brains can have maximum functionality at minimal metabolic energy cost [19, 38, 39, 40]. In other words, functional connectivity can switch with high efficiency between globally integrated and locally segregated activities. At the same time, however, it makes brain activity

vulnerable to metabolic disruptions. Small decreases in Λ lead to a sharp loss in integrated activity, which may contribute to the cognitive deficits seen in older age.

Data and code availability

Lifespan fMRI data are publicly available from Cam-CAN [21]. Metabolic fMRI data are located at Data Archive for the Brain Initiative (DABI: https://dabi.loni.usc.edu/explore/project/42) in the Protecting the Aging Brain (PAgB), Project 1926781 repository. Additional details (including links to custom MATLAB and Python codes used in the processing and analyses of data) can be found at http://www.lcneuro.org/software-and-instrumentation.

Acknowledgments and Funding

The research was funded by the WM Keck Foundation (LRMP, KD), the NSF BRAIN Initiative (LRMP, KD: ECCS1533257, NCS-FR 1926781), and the Stony Brook University Laufer Center for Physical and Quantitative Biology (KD).

CRediT authorship contribution statement

LRMP designed the experiments. AA pre-processed the data. CW did the modeling and designed the methods used. CW, LRMP, and KD wrote and revised the paper.

Declarations of interest

None.

References

[1] Jessica R Andrews-Hanna, Abraham Z Snyder, Justin L Vincent, Cindy Lustig, Denise Head, Marcus E Raichle, and Randy L Buckner. Disruption of large-scale brain systems in advanced aging. *Neuron*, 56(5):924–935, 2007.

[2] Linda Geerligs, Remco J Renken, Emi Saliasi, Natasha M Maurits, and Monicque M Lorist. A brain-wide study of age-related changes in functional connectivity. *Cerebral cortex*, 25(7):1987–1999, 2015.

[3] Sophie Achard and Ed Bullmore. Efficiency and cost of economical brain functional networks. *PLoS Comput Biol*, 3(2):e17, 2007.

[4] Lisa Mosconi. Glucose metabolism in normal aging and alzheimers disease: methodological and physiological considerations for pet studies. *Clinical and translational imaging*, 1(4):217–233, 2013.

[5] Manu S Goyal, Andrei G Vlassenko, Tyler M Blazey, Yi Su, Lars E Couture, Tony J Durbin, Randall J Bateman, Tammie L-S Benzinger, John C Morris, and Marcus E Raichle. Loss of brain aerobic glycolysis in normal human aging. *Cell metabolism*, 26(2):353–360, 2017.

[6] Christian-Alexandre Castellano, Scott Nugent, Nancy Paquet, Sébastien Tremblay, Christian Bocti, Guy Lacombe, Helene Imbeault, Eric Turcotte, Tamas Fulop, and Stephen C Cunnane. Lower brain 18f-fluorodeoxyglucose uptake but normal 11c-acetoacetate metabolism in mild alzheimer's disease dementia. *Journal of Alzheimer's Disease*, 43(4):1343–1353, 2015.

[7] Ed Bullmore and Olaf Sporns. The economy of brain network organization. *Nature Reviews Neuroscience*, 13(5):336–349, 2012.

[8] Louis A Profenno, Anton P Porsteinsson, and Stephen V Faraone. Meta-analysis of alzheimer's disease risk with obesity, diabetes, and related disorders. *Biological psychiatry*, 67(6):505–512, 2010.

[9] Daihong Liu, Lihua Chen, Shanshan Duan, Xuntao Yin, Wu Yang, Yanshu Shi, Jiuquan Zhang, and Jian Wang. Disrupted balance of long-and short-range functional connectivity density in type 2 diabetes mellitus: A resting-state fmri study. *Frontiers in Neuroscience*, 12:875, 2018.

[10] Andrew Zalesky, Alex Fornito, Luca Cocchi, Leonardo L Gollo, and Michael Breakspear. Time-resolved resting-state brain networks. *Proceedings of the National Academy of Sciences*, 111(28):10341–10346, 2014.

[11] Karl J Friston. Modalities, modes, and models in functional neuroimaging. *Science*, 326(5951):399–403, 2009.

[12] Olaf Sporns. Network attributes for segregation and integration in the human brain. *Current opinion in neurobiology*, 23(2):162–171, 2013.

[13] Dardo Tomasi, Gene-Jack Wang, and Nora D Volkow. Energetic cost of brain functional connectivity. *Proceedings of the National Academy of Sciences*, 110(33):13642–13647, 2013.

[14] Dardo Tomasi and Nora D Volkow. Aging and functional brain networks. *Molecular psychiatry*, 17(5):549–558, 2012.

[15] Réka Albert and Albert-László Barabási. Statistical mechanics of complex networks. *Reviews of modern physics*, 74(1):47, 2002.

[16] Marieke L Schölvinck, Alexander Maier, Q Ye Frank, Jeff H Duyn, and David A Leopold. Neural basis of global resting-state fmri activity. *Proceedings of the National Academy of Sciences*, 107(22):10238–10243, 2010.

[17] Li Zhao, David C Alsop, John A Detre, and Weiying Dai. Global fluctuations of cerebral blood flow indicate a global brain network independent of systemic factors. *Journal of Cerebral Blood Flow & Metabolism*, 39(2):302–312, 2019.

[18] Gasper Tkacik, Elad Schneidman, II Berry, J Michael, and William Bialek. Spin glass models for a network of real neurons. *arXiv preprint arXiv:0912.5409*, 2009.

[19] Thierry Mora and William Bialek. Are biological systems poised at criticality? *Journal of Statistical Physics*, 144(2):268–302, 2011.

[20] Elad Schneidman, Michael J Berry, Ronen Segev, and William Bialek. Weak pairwise correlations imply strongly correlated network states in a neural population. *Nature*, 440(7087):1007–1012, 2006.

[21] Jason R Taylor, Nitin Williams, Rhodri Cusack, Tibor Auer, Meredith A Shafto, Marie Dixon, Lorraine K Tyler, Richard N Henson, et al. The cambridge centre for ageing and neuroscience (cam-can) data repository: structural and functional mri, meg, and cognitive data from a cross-sectional adult lifespan sample. *Neuroimage*, 144:262–269, 2017.

[22] Lilianne R Mujica-Parodi, Anar Amgalan, Syed Fahad Sultan, Botond Antal, Xiaofei Sun, Steven Skiena, Andrew Lithen, Noor Adra, Eva-Maria Ratai, Corey Weistuch, et al. Diet modulates brain network stability, a biomarker for brain aging, in young adults. *Proceedings of the National Academy of Sciences*, 117(11):6170–6177, 2020.

[23] Kiyotaka Sato, Y Kashiwaya, CA Keon, N Tsuchiya, MT King, GK Radda, B Chance, K Clarke, and RL Veech. Insulin, ketone bodies, and mitochondrial energy transduction. *The FASEB Journal*, 9(8):651–658, 1995.

[24] Daniel J DeDora, Sanja Nedic, Pratha Katti, Shafique Arnab, Lawrence L Wald, Atsushi Takahashi, Koene RA Van Dijk, Helmut H Strey, and Lilianne R Mujica-Parodi. Signal fluctuation sensitivity: An improved metric for optimizing detection of resting-state fmri networks. *Frontiers in Neuroscience*, 10:180, 2016.

[25] Alexandre Abraham, Fabian Pedregosa, Michael Eickenberg, Philippe Gervais, Andreas Mueller, Jean Kossaifi, Alexandre Gramfort, Bertrand Thirion, and Gaël Varoquaux. Machine learning for neuroimaging with scikit-learn. *Frontiers in neuroinformatics*, 8:14, 2014.

[26] Jaime S Ide, Sanja Nedic, Kin F Wong, Shmuel L Strey, Elizabeth A Lawson, Bradford C Dickerson, Lawrence L Wald, Giancarlo La Camera, and Lilianne R Mujica-Parodi. Oxytocin attenuates trust as a subset of more general reinforcement learning, with altered reward circuit functional connectivity in males. *Neuroimage*, 174:35–43, 2018.

[27] Andre Altmann, Bernard Ng, Susan M Landau, William J Jagust, and Michael D Greicius. Regional brain hypometabolism is unrelated to regional amyloid plaque burden. *Brain*, 138(12):3734–3746, 2015.

[28] Gašper Tkačik, Olivier Marre, Dario Amodei, Elad Schneidman, William Bialek, Michael J Berry, et al. Searching for collective behavior in a large network of sensory neurons. *PLoS computational biology*, 10(1), 2014.

[29] R Matthew Hutchison, Thilo Womelsdorf, Elena A Allen, Peter A Bandettini, Vince D Calhoun, Maurizio Corbetta, Stefania Della Penna, Jeff H Duyn, Gary H Glover, Javier Gonzalez-Castillo, et al. Dynamic functional connectivity: promise, issues, and interpretations. *Neuroimage*, 80:360–378, 2013.

[30] James M Shine, Oluwasanmi Koyejo, Peter T Bell, Krzysztof J Gorgolewski, Moran Gilat, and Russell A Poldrack. Estimation of dynamic functional connectivity using multiplication of temporal derivatives. *NeuroImage*, 122:399–407, 2015.

[31] Mingrui Xia, Jinhui Wang, and Yong He. Brainnet viewer: a network visualization tool for human brain connectomics. *PloS one*, 8(7):e68910, 2013.

[32] Julia J Harris, Renaud Jolivet, and David Attwell. Synaptic energy use and supply. *Neuron*, 75(5):762–777, 2012.

[33] Simonetta Camandola and Mark P Mattson. Brain metabolism in health, aging, and neurodegeneration. *The EMBO journal*, 36(11):1474–1492, 2017.

[34] Fei Yin, Alberto Boveris, and Enrique Cadenas. Mitochondrial energy metabolism and redox signaling in brain aging and neurodegeneration. *Antioxidants & redox signaling*, 20(2):353–371, 2014.

[35] Dimitrios Kapogiannis and Mark P Mattson. Disrupted energy metabolism and neuronal circuit dysfunction in cognitive impairment and alzheimer's disease. *The Lancet Neurology*, 10(2):187–198, 2011.

[36] Yuri Geinisman, Leyla de Toledo-Morrell, Frank Morrell, Inna S Persina, and Marvin Rossi. Age-related loss of axospinous synapses formed by two afferent systems in the rat dentate gyrus as revealed by the unbiased stereological dissector technique. *Hippocampus*, 2(4):437–444, 1992.

[37] Thomas C Foster and Christopher M Norris. Age-associated changes in ca2+-dependent processes: Relation to hippocampal synaptic plasticity. *Hippocampus*, 7(6):602–612, 1997.

[38] John M Beggs. The criticality hypothesis: how local cortical networks might optimize information processing. *Philosophical Transactions of the Royal Society A: Mathematical, Physical and Engineering Sciences*, 366(1864):329–343, 2008.

[39] Luca Cocchi, Leonardo L Gollo, Andrew Zalesky, and Michael Breakspear. Criticality in the brain: A synthesis of neurobiology, models and cognition. *Progress in neurobiology*, 158:132–152, 2017.

[40] Dante R Chialvo. Emergent complex neural dynamics. *Nature physics*, 6(10):744–750, 2010.